Numerical Analysis and Design of New Exhaust Section Downstream of Constant Volume Combustor

(Article begins on next page)

19 October 2024

NUMERICAL ANALYSIS AND DESIGN OF NEW EXHAUST SECTION DOWNSTREAM OF CONSTANT VOLUME COMBUSTOR

Panagiotis Gallis
PhD Student
Department of Energy
Politecnico di Torino
Turin, Corso Duca degli Abruzzi, 24–10129
Email: panagiotis.gallis@polito.it

Daniela Anna Misul *
Associate Professor
Department of Energy
Politecnico di Torino
Turin, Corso Duca degli Abruzzi, 24–10129
Email: daniela.misul@polito.it

Bastien Boust
Research engineer
Pprime Institute
CNRS-ENSMA–University of Poitiers,
Poitiers, Avenue Clément Ader, 1–86961,
Email: bastien.boust@ensma.fr

Marc Bellenoue
Full Professor
Pprime Institute
CNRS-ENSMA–University of Poitiers,
Poitiers, Avenue Clément Ader, 1–86961,
Email: marc.bellenoue@ensma.fr

Simone Salvadori
Assistant Professor
Department of Energy
Politecnico di Torino
Turin, Corso Duca degli Abruzzi, 24–10129
Email: simone.salvadori@polito.it

ABSTRACT

Pressure Gain Combustors (PGC) exploit either their isochoric or detonative combustion increasing the theoretical thermal efficiency of a Gas Turbine cycle. On this basis, a Constant-Volume Combustor (CVC) is developed operating with rotary valves while the chamber is fed with mixture of air and liquid iso-octane. The present work describes the numerical design of a new exhaust section after the CVC. First, the design parametrization of the transition duct and the resulting Design of Experiments (DOE) of 81 samples are

∗corresponding author

introduced. Every case is numerically tested and the election of the best sample is based on the pressure losses and the oscillations characterization. In the last part, the LS89-VKI vane is added at the aft part of the best transition duct and the ensemble exhaust system is analysed with the help of transient CFD analysis. Every component is evaluated in terms of pressure losses and oscillations, while the operation of the vane is investigated in details. The results of the stator's performance are discussed and compared with steady experimental data. During a CVC period, the cycle average outlet flow angle remains close to the outlet metal angle denoting promising results for the future numerical analysis of the subsequent rotor.

NOMENCLATURE

Roman letters

A Area $[m^2]$

C Chord $[m]$

f Frequency $[Hz]$

L Length $[m]$

$\dot{m}$ Massflow Rate $[kg/s]$

P Static Pressure $[Pa]$

P_t Total Pressure $[Pa]$

R Radius $[m]$

T Static Temperature $[K]$

t Time $[s]$

T_{period} Time Period $[s]$

T_t Total Temperature $[K]$

u Velocity $[m/s]$

Greek letters

α^o Flow Angle $[deg]$

ρ Density $[kg/m^3]$

2

Journal of Engineering for Gas Turbines and Power

τ Integration Time $[s]$

    Dimensionless groups

ζ_{α^o} Flow Angle Deviation Coefficient $[-]$

ζ_{P_t} Total Pressure Losses $[-]$

ζ_v Loss Coefficient $[-]$

AR Aspect Ratio $[-]$

$\hat{C}$ Cross-Correlation Coefficient $[-]$

D Damping Factor $[-]$

G Objective Function $[-]$

GCI Grid Convergence Index $[-]$

Ma Mach number $[-]$

N Number $[-]$

R Range $[-]$

Re Reynolds Number $[-]$

S_R Steepness of Endwalls $[-]$

    Superscripts and subscripts

1 Inlet of Vane

2 Outlet of Vane

$\hat{}$ Reduced

CA Cycle Average

CVC Constant Volume Combustor

ex Outlet

in Inlet

$is.$ Isentropic

MA Mass Weighted Average

T Transition Duct

t Total

WA Work Average

3

back   Outlet of Domain

Duct-Out   Transition Duct Outlet

SA Split Average

   Acronyms

BC   Boundary Conditions

CO   Component Evaluation

CP   Control Point

CU   Cumulative Evaluation

CVC   Constant Volume Combustor

DOE   Design of Experiments

DOF   Degree of Freedom

HPT   High-Pressure Turbine

IGV   Inlet Guide Vanes

JP   Junction Point

L   Left Vane

P   Periodic Vane

PDE   Pulse Detonation Engine

PGC   Pressure Gain Combustion

PS   Pressure Side

R   Right Vane

RANS   Reynolds–Averaged Navier–Stokes

RDE   Rotating Detonation Engine

SEC   Sockless Explosion

SS   Suction Side

URANS   Unsteady Reynolds–Averaged Navier–Stokes

4

1   INTRODUCTION

In recent times, the Pressure Gain Combustion (PGC) technology came under the spotlight thanks to their advantageous performance compared to the conventional burners of Gas Turbine cycles. PGC cycles offer a rise of the stagnation pressure during the combustion process accompanied by an elevated inlet temperature for the subsequent expander. Thus, the theoretical cycle efficiency of PGC achieves higher levels comparing the traditional Joule cycle [1, 2, 3] . This interesting evidence is more distinct in operating points with low pressure ratio [4]. Therefore for the same power demand, PGC cycle could provide a Gas Turbine with less weight and specific fuel consumption contributing to the reduction of economical and environmental cost.

These unconventional machines are split into two major families. The principal of this division emerges from the nature of the combustion. PGC technologies either exploit the harsh and violent detonative process or the isochoric deflegrative combustion [5, 6]. The most notable representatives of the detonative family are the Pulse Detonation Engine [7] (PDE) and the Rotating Detonation Engine [8, 9, 10] (RDE). On the other hand, the deflegrative solution includes the Wave Rotor [11] and the Shockless Explosion (SEC) [12]. Within the category of deflegrative combustors, Boust *et al.* [13] developed a prototype Constant Volume Combustor (CVC) which achieves a sequential iso–choric combustion with the help of two pairs of rotary inlet and outlet valves. In particular, pressurised hot air in appropriate conditions is guided inside a chamber, while the inlet valves are open. Later, liquid iso–octane is directly injected inside the chamber, during the moments when both inlet and outlet valves are closed. With a help of a spark–plug ignitor constant volume combustion occurs raising significantly the stagnation properties of the medium. In the end, the exhaust ports open and the burned gas are expanded through the outlet system, which is consisted of a rectangular plenum coupled with a converging–diverging circular nozzle. An extensive analysis using Large Eddy simulations [14] uncovered the dominant role of the local spark timing velocity and the residual burned gases on the operational variability of the machine. Concerning the exhaust system, a large experimental campaign [15] was conducted offering a parametric study of the CVC performance for various operating frequencies, plenum sizes and nozzle throat diameters. Moreover, a validated 1D model [16, 17] of the ensemble test rig can

5

Journal of Engineering for Gas Turbines and Power

offer the outlet conditions of CVC, which are challenging to measure.

The current activity attempts to examine the re–design of an exhaust system downstream of CVC to connect it with a High–Pressure Turbine (HPT) stage. Nonetheless, this unconventional machine has never been investigated concerning its possible integration with a subsequent turbine module. The research activities relating to this PGC revolved around the architecture, operation and performance of the combustion system. On the contrary, there is a chasm regarding the characterization of CVC's outflow and the HPT stage performance attached downstream of CVC. Thus, this study proposes a numerical methodology to investigate the performance of the CVC connection with Inlet Guide Vanes (IGV) for the first time in literature. For that reason, it is essential to enumerate previous efforts of turbine integration to a PGC with similar flow unsteadiness. The PGC which is chosen to serve as a precursor of the current CVC exhaust study is the PDE. The similarities of the two PGC's exhaust conditions rely on the solely axial outflow, the morphology of a spike pulsation and the similar levels of low operational frequency between PDE and CVC. In particular, the operational frequency of PDE ranges at few to hundreds of Hertz [6]. For a conventional transonic HPT vane, PDE's range of pulsation limits the reduced frequency of the vane below unity. For the current analysis of CVC, the reduced frequency is below 0.5. Thus, the two combustors produce a dynamic flow field which at least in terms of time is very similar. This is certainly important as the reduced frequency highly affects the HPT stage performance [18]. In addition, the elevated total pressure inside the chamber of CVC and the combustion tube of the PDE provides a supersonic outflow. However, there is a difference between the amplitude of the pulsation between the two cases, as CVC is characterised by sequential deflegrative events, whereas PDE emits periodically detonative waves. Nevertheless, the produced outflow of two machines are in general very similar.

Many interesting experimental campaigns tried to shed the light on the interactions between a PDE and a HPT stage. Glaser *et al.* [19] performed experiments of a PDE followed by an axial HPT stage. They presented the effect of fill fraction, equivalence ratio and rotor speed on the performance of turbine. Later, they managed to map the turbine's performance under different frequencies of pulsation stressing the importance of corrected mass flow variation compared to the

6

frequency on the turbine's efficiency [20]. Moreover, they underlined that the poor turbine's performance arose by the variation of the rotor incidence due to the sequential firing of PDE's tubes [21]. Fernelius *et al.* [22, 23] attempted to mimic the pulsation of PDE by expanding pressurized air though a rotating ball valve to a turbine. They demonstrated that increasing the frequency, the efficiency of the expander approached the steady case for different pressure ratios. Afterwards, they conducted CFD analysis that were validated with the help of preceding experimental campaigns. The frequency range of the analysis was $[10 - 40]\ Hz$. They indicated the importance of the amplitude and not frequency to the efficiency deficit. In addition, the rotor incidence angle was the major parameter of the turbine's performance reduction under pulsating inflow. Moreover, they tried to optimize through multi–point method the turbine under pulsation. Results indicated that a rotor blade with less turning seemed to be more unaffected by the pulsation. Concerning other numerical activities, Ni *et al.* [24] analysed a turbine stage after PDE for different pulsation types. The stage performance was compared between a pulsation by the simultaneous opening of the PDE valves (synchronous) with the consecutive azimuthal opening of them (sequential). They demonstrated the superiority of a synchronous pulsation over a sequential one, since significant losses were induced due to the spillage of energy in different passages. Xisto *et al.* [25] performed a CFD analysis of multiple PDEs coupled with a HPT axial stage. In particular, they described thoroughly the flow field and stressed the influence on the stage efficiency of purge fraction time at varying rotor speeds. Furthermore, they highlighted that the variation of rotor's incidence during a cycle triggered flow separation occurring alternately on the suction and pressure sides of the blades. Liu *et al.* [26, 18] numerically analysed a HPT stage under axial pulsation for different inlet Mach numbers by modifying the hub–tip endwalls shape upstream of the vane. In fact, the inlet flow area of the vane was reduced, while the span of the vane remained the same. Diffusive hub and tip endwalls connected the inlet with the stator passage. Thus, the contraction ratio of the vane was changed by changing the inlet area and the inlet Mach number was accordingly elevated. The diffusive endwalls generated separation zones at the inlet hub and tip regions upstream of the vane. They demonstrated that larger inlet Mach number attenuated more the pulsation as the induced separated flow acted as a damper to the flow field.

7

The topic of the present activity is the design of a transition duct between the CVC and a HPT vane. First, the overview of the conceptual design of the machine is presented. The exhaust plenum of the existing experimental test rig is preserved to the new exhaust system. On the other hand, the circular converging–diverging nozzle is replaced by the transition duct and a HPT vane cascade downstream. After describing the function and the dimensioning of the major parts, the analysis focuses on the transition duct. In particular, a parametric numerical study of different design samples is accomplished. The parametrization of the transition duct and the resulting Design of Experiments (DOE) are thoroughly described. The transient CFD parametric study of the DOE reveals the sample that offers the best compromise between total pressure losses and oscillations. A straight comparison of the cycle flow field of the best and worst case is shown. In fact, the best sample serves as a transition duct of the new exhaust system for the second part of the activity. Thus, this specific component is able to couple the CVC exhaust with the HPT vane. The VKI LS-89 airfoil profile is used for the purposes of the current study as an annular cascade. The unsteady numerical calculations of the 3D ensemble domain offers the flow field analysis of the vane under a CVC pulsation. In particular, the evaluation of vane's aerodynamic performance under oscillating flow field is discussed, while the total pressure losses and the oscillating behaviour of all components are highlighted. The choice of stagnation pressure as a flow property to measure the performance of the exhaust system is of the essence for the current analysis. In particular, the major advantage of PGC machines, such as CVC, is the rise of the total pressure during the combustion process. Thus, it is necessary to address the morphology of stagnation pressure signals downstream of CVC. The current work attempts to investigate for the first time a stator's performance under the influence of the CVC exhaust conditions providing interesting findings for the conditions of a subsequent rotor.

2 CONCEPTUAL DESIGN OF NEW EXHAUST SYSTEM

The conceptual design of the new exhaust system is portrayed in Fig. 1. In particular, the major components of the system can be identified in Fig. 1ii). First of all, the rectangular straight plenum (*a*) of the existing experimental test rig [15] is placed. Nonetheless, the converging–diverging noz-
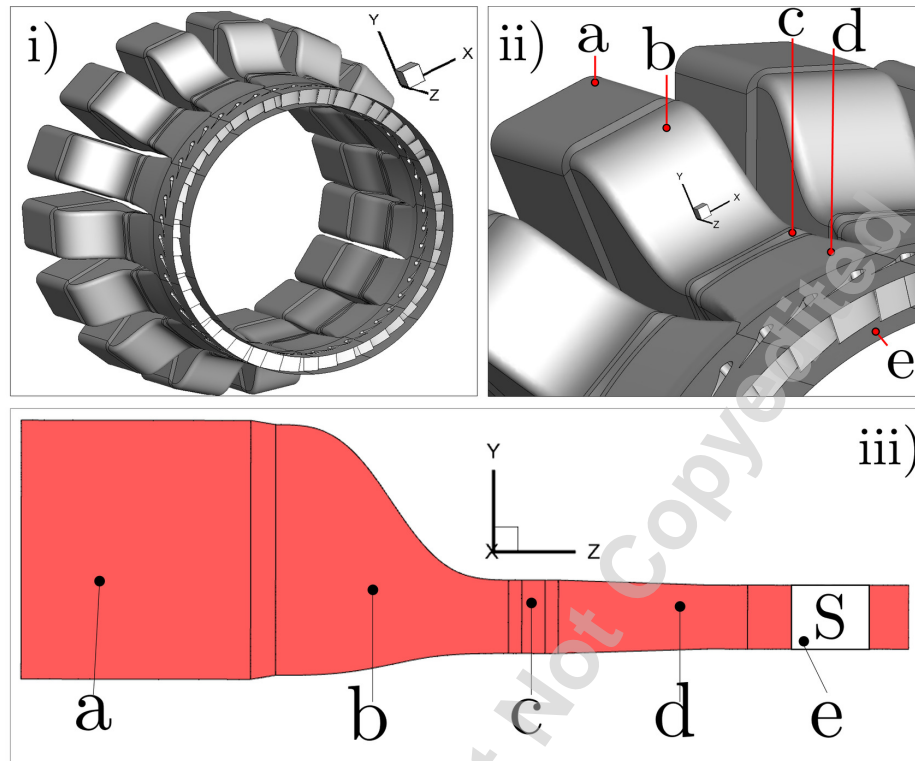
8

Fig. 1.   CONCEPTUAL DESIGN OF NEW EXHAUST SYSTEM

zle downstream of the plenum at the current experimental configuration is not preserved. On the contrary, the plenum is followed by the transition duct (*b*) which helps to attenuate the oscillating flow without inserting considerable losses to the system. The straight rectangular cross–section by *b* evenly changes to an annular cross–section through *c*. Afterwards, the annular section increases its angle by decreasing its span through *d* preserving the same cross section area. This component is named angular duct. Finally, the Inlet Guide Vanes (IGVs) are placed in the end of the domain (*e*).

As it can be observed, a configuration of $15 : 45$ between the CVCs and vanes is chosen. The existing CVC exhaust system configuration consists of the rectangular straight plenum (*a*) coupled with a circular converging–diverging nozzle [15]. The design of the nozzle is based on the ISO 9300:2005 with $20\ mm$ diameter. On the other hand, the chosen profile of IGVs for the new exhaust system is the LS–89 VKI profile [27, 28] of a linear experimental cascade. For the purposes of the current annular cascade, this profile is selected because it fits the characteristics

9

Journal of Engineering for Gas Turbines and Power

Table 1.   GEOMETRICAL FEATURES OF NEW EXHAUST SYSTEM

N_{CVC}	N_{Vanes}	R_{Shaft}	C	AR
15 [-]	45 [-]	150 [mm]	24.64 [mm]	0.781 [-]

of a typical HPT vane, it is publicly available and its performance results have been thoroughly

described and can be used as a benchmark for comparative studies for different inlet conditions.

The main geometrical characteristics of domain are presented in Table 1. The selection of the

number of vanes, the shaft radius and the chord of the blade are appropriately elected. The

criteria of these choices are two. First of all, the new exhaust system minimum area offered by

the annular cascade is equal to fifteen times the throat nozzle area of the existing outtake system

of CVC. Thus, the operating point with respect the experimental analysed CVC does not change

for the fifteen combustors of the configuration in Fig. 1. CVC combustor chamber will operate

the same way with the old existing and new exhaust system. The second criterion is based on

providing vanes with reasonable values of aspect ratio for a HPT stage $(0.7 - 1)$.

3   DESIGN OF TRANSITION DUCT

In this part, the methodology of the transition duct design is described in details. First, in the

Section 3.1 the parametrization of the meridional profile of the transition duct and the produced

DOE are presented. In Section 3.2, the appropriate transient inlet Boundary Conditions (BCs),

which will be inserted to each sample of DOE, are reported. Later, in Section 3.3 the numerical

configuration of the simulations are introduced, while at Section 3.4 the evaluation strategy of all

the samples is presented. In the end, at Section 3.5 the DOE results followed by a flow field

comparison of worst and best samples are presented.

3.1   Parametrization and DOE

In Fig. 2, the meridional profile of the baseline transition duct can be identified. The axis

are placed in non-dimensional form with the help of the length of the transition duct (L_T) which

is kept constant. The duct's endwalls are consisted of two splines which are constructed with
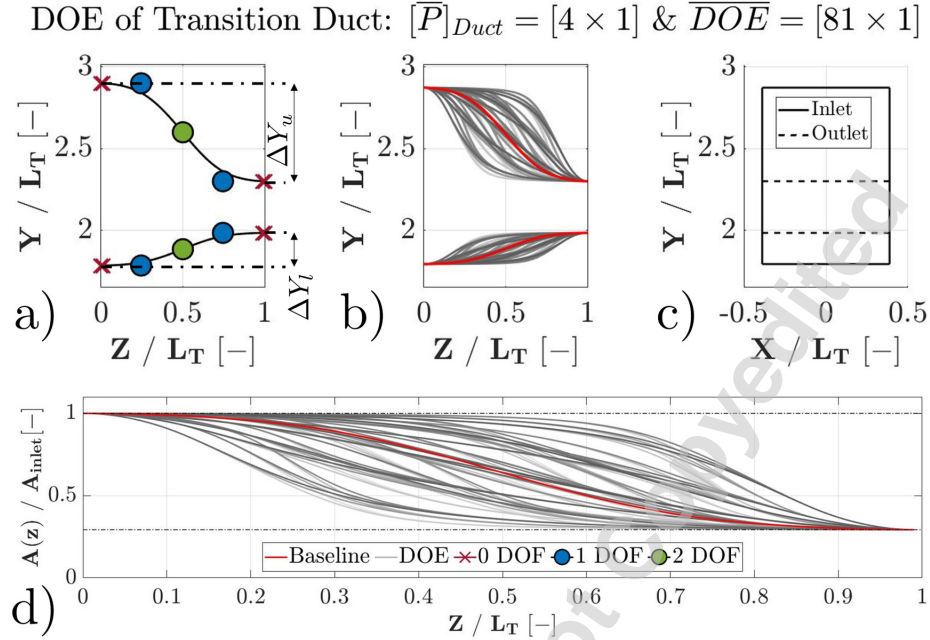
10

Fig. 2.   PARAMETRIZATION AND DOE OF TRANSITION DUCT

the help of seven control points (CP) each. In particular, the three middle control points of each spline are variable, while only the middle point have two degrees of freedom (DOF). The variable control points of upper and lower splines have the same properties, despite the fact that they are not axis–symmetric with respect the mean–line of the meridional plane. The axial (z–axis) positions of the upper and lower control points can take identical values. On the other hand, the inlet fixed control points have different inner and outer vertical location with respect the outlet fixed control points. As a result, the vertical distance between the upper inlet fixed control point and the upper outlet fixed control point (ΔY_u) is different than the distance between the lower inlet fixed control point and the lower outlet fixed control point (ΔY_l). Thus, a design can be defined by solely altering the position of the variable control points of the upper spline and insert the same variables re–scaled to the vertical distance ΔY_l of the lower spline. Therefore, in total a sample is reproduced with four parameters.

In Fig. 2b, the samples of the DOE are depicted, along with the baseline design coloured in red. The full factorial design method of 3 levels is chosen. A sample is introduced with the help of 4 parameters. Consequently, the DOE consists of 81 geometries ($3^4 = 81$). The allowed levels of

11

Table 2.   FULL FACTORIAL DESIGN OF 3 LEVELS

Parameter	1st	2nd	Level 1	Level 2	Level 3
1	Point A	Point B	0.3	0.5	0.7
2	Point A	Point B	0.1	0.5	0.9
3	Point A	Middle CP	0.3	0.5	0.7
4	Middle CP	Point B	0.3	0.5	0.7

each parameter are defined at Table 2. It must be underlined that Parameter 1 is defined the axial

position (z–axis) of the middle point (Middle CP), whereas Parameter 2 corresponds to its vertical

position (y-axis). Starting from the inlet, Parameter 3 is named the axial position of the first variable

control point and Parameter 4 the axial position of the last variable control point. In addition, the

first fixed control point is defined as Point A and the last fixed control point is named Point B. As a

result, the axial distance of Point A and Point B is equal to the length of the transition duct, which

remains constant for all the samples. These names are used for both cases of lower and upper

splines. The values of level (4-6 columns) are referred to the fraction of the distance between

the points of the 2nd and 3rd columns. The following two examples will aid to fully understand the

structure and the meaning of Table 2. If the Parameter 3 takes the Level 2 value, the axial position

of the first variable control point of the lower and upper spline will be placed at 50 % of the length

of the duct. In addition, if the Parameter 2 obtains the value of Level 3, the lower control point

will be placed at the 90 % of ΔY_l and the upper control point at 90 % of ΔY_u. It must be noted

that the baseline geometry is derived by imposing the second level values to all the parameters

respectively.

Table 3.   STEEPNESS EVALUATION OF SAMPLES

Example	$|S_R|$		Category
a	0.03	[-]	Linear
b	0.06	[-]	Baseline
c	0.15	[-]	Steep

12

Table 4. LOAD EVALUATION OF SAMPLES

Example	S_R	Category
d	0.15 [-]	Forward
e	0 [-]	Central
f	-0.14 [-]	Backward

In Fig. 2c, a sectional view from the inlet can be seen. As a consequence, the parametrization indeed varies the transition duct profile only to the meridional plane preserving constant inlet and outlet cross—section areas for all samples. In Fig. 2d the varying area ratio profiles of each sample are placed. This graph demonstrates that each sample decreases the area along the axial distance of the duct ensuring that a continuous acceleration will take place in the exhaust domain. It is not noticed any anomaly or any alternation between acceleration and diffusion of the samples ensuring the smooth and continuous acceleration of the flow field. Nevertheless, the gradient of this acceleration differs and it will be evaluated for each sample.

It is certainly useful to group the sample geometries into different categories. The characteristic which serves as a criterion of this categorization is the steepness of the constructive spline of the samples. If one calculates the resulting area S_R of a spline with its linear projection (e.g. grey shaded area of Fig. 3d), then two considerations can be made:

1. $|S_R|$: The absolute value of this property indicates how fast the endwall changes. Hence, this can serve as a metric of steepness, as it can be seen in the pink shaded regions of Fig. 3a, b and c. The values of these examples are inserted at Table 3. If this metric has large values, then the geometry is characterized as steep. On the contrary, if the absolute value of this area is small, then the sample is identified as linear.

2. S_R: On the other hand, the value of this area indicates if the change of gradient occurs up-stream or downstream of the middle point. Thus, this can serve as a metric of backward, central or forward loaded samples, as it can be seen in Fig. 3d, e and f. The values of these examples are placed at Table 4.

13

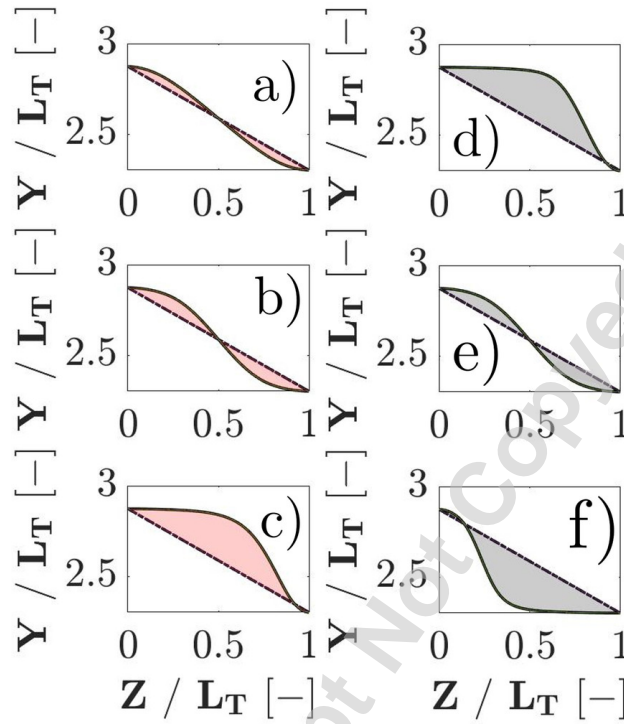## Steepness and Load Evaluation

Fig. 3.   CATEGORIZATION OF TRANSITION DUCT SAMPLES

3.2   Boundary Conditions

After the creation of a large group of samples, each geometry is tested numerically under the same pulsating inlet BCs focusing on the oscillations attenuation and the reduction of the produced losses. In other words, the evaluation of each case will be performed with an unsteady simulation. On Fig. 4a, the produced stagnation conditions retrieved by a validated 1D model [16, 17] are displayed. The axis of graph are dimensionless with the help of the inlet total pressure and temperature of CVC experimental test rig ($P_{t, in} = 3.2\ bar\ \&\ T_{t, in} = 450\ K$).

If each sample is coupled with the subsequent vane, every case would be characterized by a significant large number of elements and an increased numerical cost. An efficient solution to face this issue is the reduction of the flow domain. For the evaluation of the DOE, the flow domain of each sample is restricted only to the exhaust plenum (*a*), the transition duct (*b*) sample, the transition from rectangular to annular cross–section (*c*) and a large artificial plenum. The placement of an artificial plenum accommodates the absorption of pressure waves due to pulsating
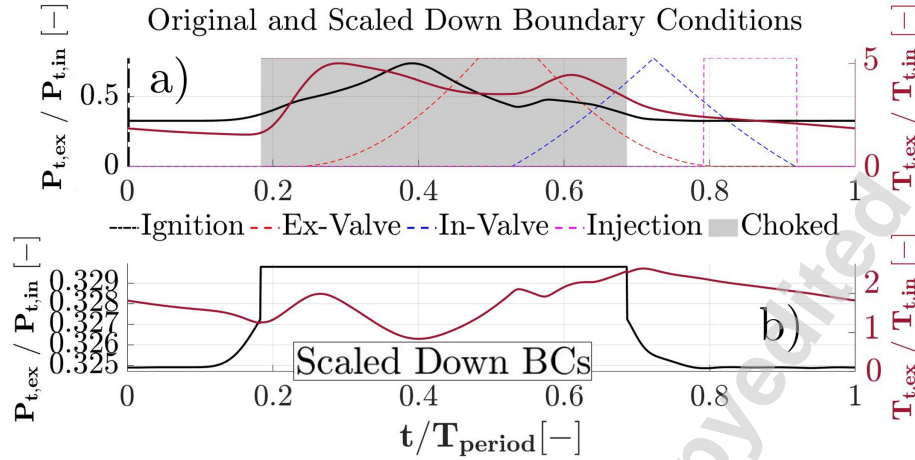
14

Fig. 4.   ORIGINAL AND SCALED DOWN EXHAUST CONDITIONS OF CVC

inflow before reaching the outlet boundary. This modified configuration of the samples makes the transition duct outlet the restricted area of the domain. As a consequence, the minimum area of the sample domain and the nozzle throat area of the existing exhaust system mismatch. By using the same inlet boundary conditions, this would lead to choked samples under specific time period of the cycle, which is inadequate with the reality. Therefore, due to the absence of the real restricted area in the domain of samples, the inlet boundary conditions of the system should be changed. By holding the same back pressure, inlet conditions should be scaled down to keep the operating point for the transition duct.

It must be underlined that the scaled down boundary conditions are not retrieved by applying a constant reducing scaling factor. Instead, the process of calculating the synthetic boundary conditions relies on preserving the same range of operating points of the transition duct for the case of ensemble exhaust system (I) and the case of reduced flow domain for the samples (II). By solving for each time step the isentropic equations of the original BCs, the Mach number at the outlet of the transition duct is kept below of 0.2. This condition is respected for the II case with the Eq. 1.

$$Ma^{I}_{Duct-Out}(t) = Ma^{II}_{Duct-Out}(t) \tag{1}$$

15

For the case of the reduced flow domain of the samples, the back–pressure is now applied at the end of the transition duct. Thus, in order to have the same Mach number the two cases the stagnation pressure must be retrieved by Eq. 3.

$$P_{Duct-Out}^{II} = P_{Back} \rightarrow$$ (2)

$$P_t^{II}(t) = \frac{P_{Duct-Out}^{II}}{(1 + \frac{\gamma-1}{2} Ma_{Duct-Out}^{II}(t)^2)^{\frac{-\gamma}{\gamma-1}}}$$ (3)

Except of the same Mach number, the system of the transition duct should be exposed in the same mass flow rate. Hence, the total temperature for the II case is determined by Eq. 4.

$$\dot{m}^I(t) = \dot{m}^{II}(t) \rightarrow T_t^{II}(t) = [P_t^{II}(t) \cdot \frac{\sqrt{T_t^I(t)}}{P_t^I(t)}]^2$$ (4)

Consequently, by scaling down the inlet stagnation BCs, the transition duct samples (II) experiences the same pressure ratio and corrected mass flow rate as the case in which the transition duct is a part of the ensemble exhaust system. The scaled down BCs are placed at Fig. 4b.

3.3 Numerical Set Up

The flow domain of each sample includes the plenum, the sample transition duct, the transition from rectangular to annular cross–section and the artificial exhaust plenum. In parallel, the current analysis exploits the existence of symmetry in the $y - z$ plane and only the half of the referred volume is analysed. In Fig. 5, the meshed volume of $1.8\ 10^6$ elements is depicted in various views.

The colours of the faces are in correspondence with the Table. 5.
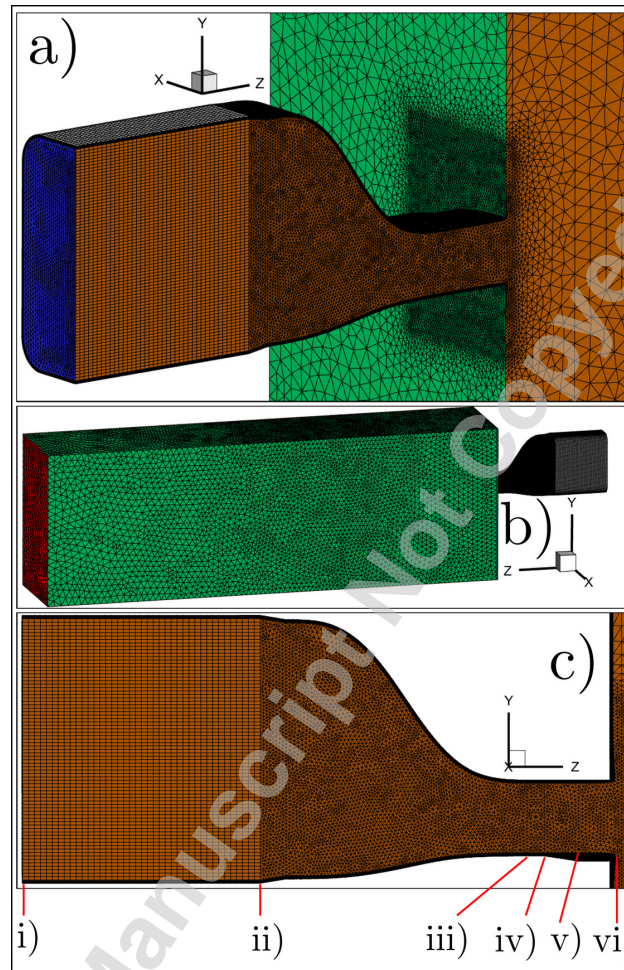

Fig. 5.   MESHED VOLUME OF TRANSITION DUCT SAMPLES

The medium is considered ideal gas, the cycle average heat capacity at constant pressure and
molecular weight are inserted, while the dynamic viscosity is calculated with the Sutherland Law.
The commercial 2nd order accurate density–based implicit solver of FLUENT by ANSYS is used to
solve the Unsteady Reynolds–Averaged Navier–Stokes (URANS) equations of the domain. The
turbulence model of $k - \omega$ proposed by Wilcox [29] is preferred. Inflation layer close to viscous
walls is added to the meshed volume ensuring a y^+ below 1 during the calculations. The cycle
period of CVC is $25\ Hz$, while the sampling frequency of the solver is modified to $12.5\ kHz$ so as

17

Boundary Conditions	
Type	Properties
Inlet	Scaled: $P_t(t)$ & $T_t(t)$
Outlet	$P = 1 \, [atm]$
Symmetry	-
No–Slip Wall	Adiabatic
Free–Slip Wall	Adiabatic

Table 5.   BOUNDARY CONDITIONS OF SAMPLES

to analyse in high accuracy two operating cycles. A 2nd order accurate time advancement scheme with 20 sub–iterations is utilized for the purposes of the DOE analysis.

After specifying the meshed flow domain of DOE and the solver parameters, it is necessary to address the duration of the calculations for each sample. First of all, the reduced frequency of the cases can be calculated with Eq. 5. For the current PGC, the reduced frequency is below one. In other words, the pulsation varies slower than it convects through the domain of interest. Hence, it is expected that during the first cycle the pulsation has enough time to propagate through the transition duct permitting the performance evaluation to take place in the very next period.

$$\hat{f} = \frac{f_{pulsation}}{\overline{u}_{in} \, / \, L_{Domain}} = 0.416 \, [-] \tag{5}$$

In spite of the low reduced frequency, it is necessary to define a criterion for the establishment of a periodic (unsteady) convergence of the simulation. In fact, the baseline sample is tested for four periods. The mass flow rate, mass–weighted average Mach number, and mass–weighted stagnation temperature are sampled at the major locations of the sample flow domain. In particular, the locations of inlet of domain (i), inlet (ii) and outlet (iii) of transition duct, inlet (iv) and outlet (v) of the transition from rectangular to annular cross–section, and inlet of the artificial plenum (vi) are displayed in Fig. 5. In Fig. 6 the evolution of these three flow properties can be seen at the
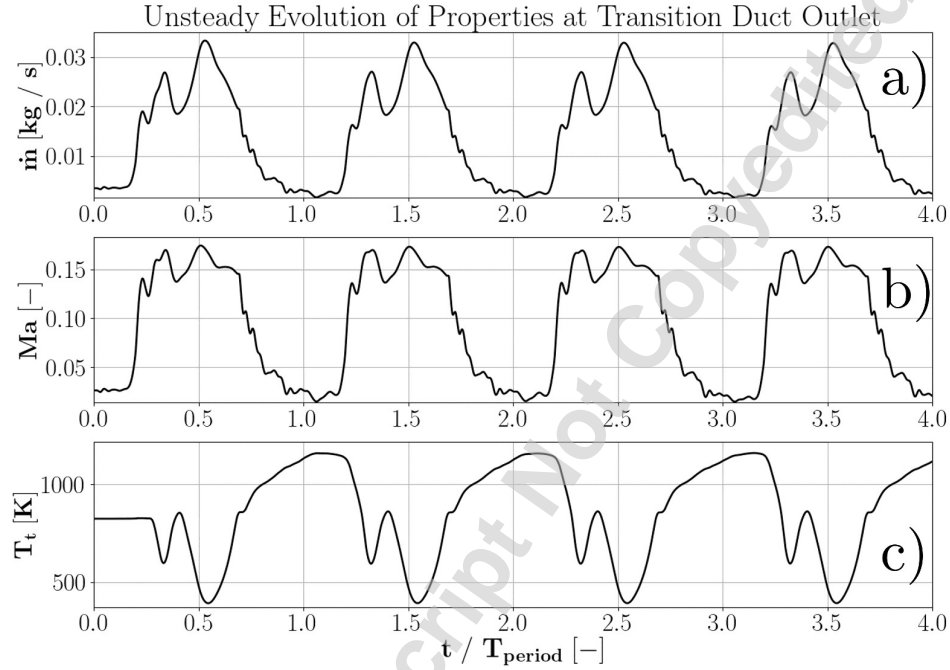
18

outlet of the transition duct (iii).

Fig. 6.   MASSFLOW, MASS–WEIGHTED MACH NUMBER AND MASS–WEIGHTED TOTAL TEMPERATURE AT THE OUTLET OF BASELINE TRANSITION DUCT

Afterwards, the cross–correlation is performed between two sequential cycles for each property of each location. The values for zero lag are placed for each flow variable in the matrices of the Eq. 6. The minimum, average and maximum values of each matrix can be deduced. These values are displayed in Fig. 7. It is observed that all the statistic variables of each flow property are above the threshold of $98\ \%$ after the second period. Thus, this analysis demonstrates that after the second cycle the periodicity is established throughout the whole flow domain of interest. In conclusion, it is considered accurate to simulate and evaluate each sample during the second resolved cycle.

19

$$\hat{C}_{\dot{m}} = \begin{bmatrix} (\hat{C}_{\dot{m}})_i \\ (\hat{C}_{\dot{m}})_{ii} \\ (\hat{C}_{\dot{m}})_{iii} \\ (\hat{C}_{\dot{m}})_{iv} \\ (\hat{C}_{\dot{m}})_v \\ (\hat{C}_{\dot{m}})_{vi} \end{bmatrix}, \ \hat{C}_{Ma} = \begin{bmatrix} (\hat{C}_{Ma})_i \\ (\hat{C}_{Ma})_{ii} \\ (\hat{C}_{Ma})_{iii} \\ (\hat{C}_{Ma})_{iv} \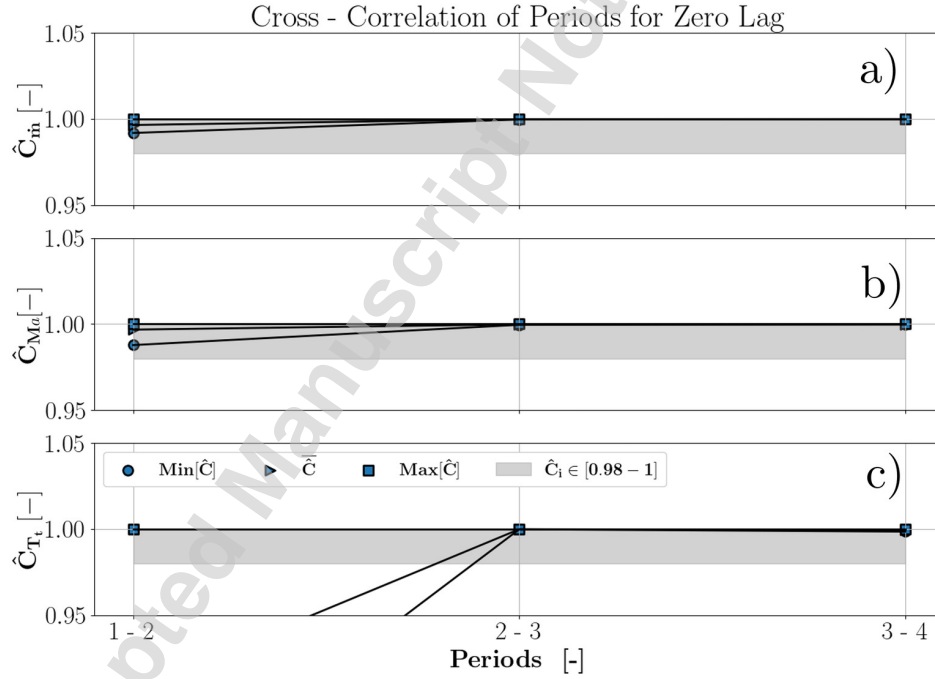\ (\hat{C}_{Ma})_v \\ (\hat{C}_{Ma})_{vi} \end{bmatrix}, \ \hat{C}_{T_t} = \begin{bmatrix} (\hat{C}_{T_t})_i \\ (\hat{C}_{T_t})_{ii} \\ (\hat{C}_{T_t})_{iii} \\ (\hat{C}_{T_t})_{iv} \\ (\hat{C}_{T_t})_v \\ (\hat{C}_{T_t})_{vi} \end{bmatrix} \tag{6}$$

Fig. 7. ESTABLISHMENT OF PERIODICITY VIA CROSS–CORRELATION CRITERION FOR BASELINE SAMPLE

3.4 DOE Evaluation

The second cycle of each sample is analysed in terms of oscillations and stagnation pressure losses. In particular, the transient signals of the mass–weighted average of the stagnation pres-

20

sure at the outlet of transition duct of each sample is monitored for each time step. For a flow property Φ, the mass–weighted average at a specific area A is deduced by Eq. 7.

$$\Phi^{MA} = \frac{\int_A \rho u \Phi \, dA}{\int_A \rho u \, dA} \tag{7}$$

The cycle total pressure losses are calculated between the inlet of the domain and the outlet of the transition duct by Eq. 8.

$$\overline{\zeta}_{P_t} = \frac{\int_0^\tau (P_t^{MA})_{Out} \, dt - \int_0^\tau (P_t^{MA})_{In} \, dt}{\int_0^\tau (P_t^{MA})_{In} \, dt} \tag{8}$$

Concerning the oscillating behaviour of each component, the reduced range [26, 18] of the transient total pressure signals at inlet of domain and outlet of transition duct are calculated. Hence, by comparing these two properties the damping factor can be computed as in Eq. 9.

$$\hat{R} = \frac{Range(P_t^{MA})}{\frac{1}{\tau}\int_0^\tau (P_t^{MA}) \, dt} \;\rightarrow\; D_{\hat{R}} = \frac{\hat{R}_{In} - \hat{R}_{Out}}{\hat{R}_{Out}} \tag{9}$$

A final metric of the performance of the samples is the G function of Eq. 10, which includes both the losses and the damping factor. This variable serves to evaluate the DOE and ranks the samples performance from the best to the worst case.

$$G = \sqrt{\frac{1}{2} \cdot (1 - \overline{\zeta}_{P_t})^2 + \frac{1}{2} \cdot sign(D_{\hat{R}}) \cdot D_{\hat{R}}^2} \tag{10}$$

21

3.5 Results

In the Fig. 8, the evaluation of DOE is displayed. The symbol of each sample represents a backward, central or forward loaded sample, while the color of each point refers to the steepness of each geometry, in accordance to Fig. 3. Every sample provides solution with excitation and not attenuation. Backward loaded sample regardless its steepness seems to probably offer higher losses with more excitation of the signal. On the other hand, central or forward loaded samples induce less losses with significant smaller level of excitation. By evaluating the G property of Eq. 10, the worst geometry is backward loaded with high steepness, while the best given sample is a forward loaded with low level of steepness.
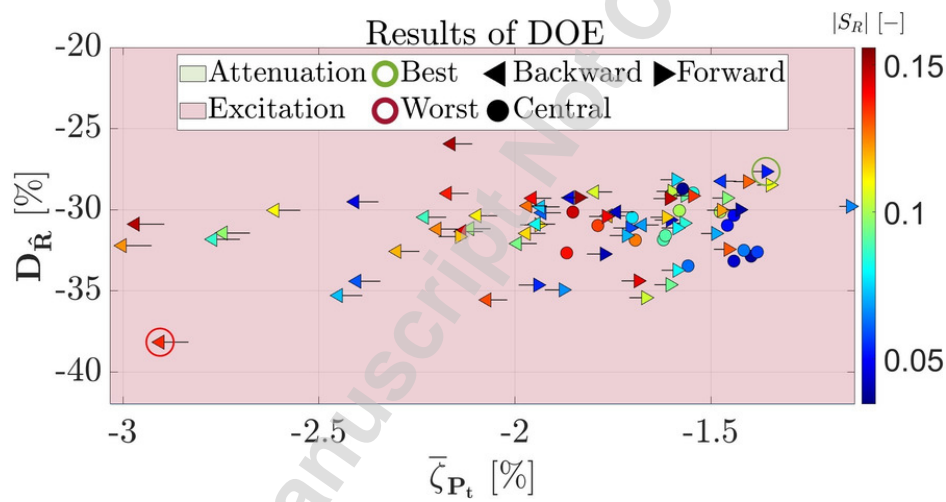
Fig. 8.   EVALUATION OF DOE SAMPLES

In Fig. 9, the flow field comparison in the meridional plane of best (B) and worst (W) geometry of DOE is introduced. The contours of Mach number and turbulent kinetic energy are used. The sequential frames are sampled at 12.5 %, 25 %, 50 %, 75 % and 87.5 % of second cycle. Without any doubt, the scaled down BCs achieved their goal, as the cyclic Mach profile of the samples respects the prescribed limits. Nevertheless, the periodic expansion of the flow in the artificial plenum adds high level of unsteadiness to the flow field domain. In particular, the generated shear flow by expansion inside the plenum does not allow for steady pressure condition at the duct's outlet. As a result, the flow field upstream of the plenum's expansion is being oscillated and the

22

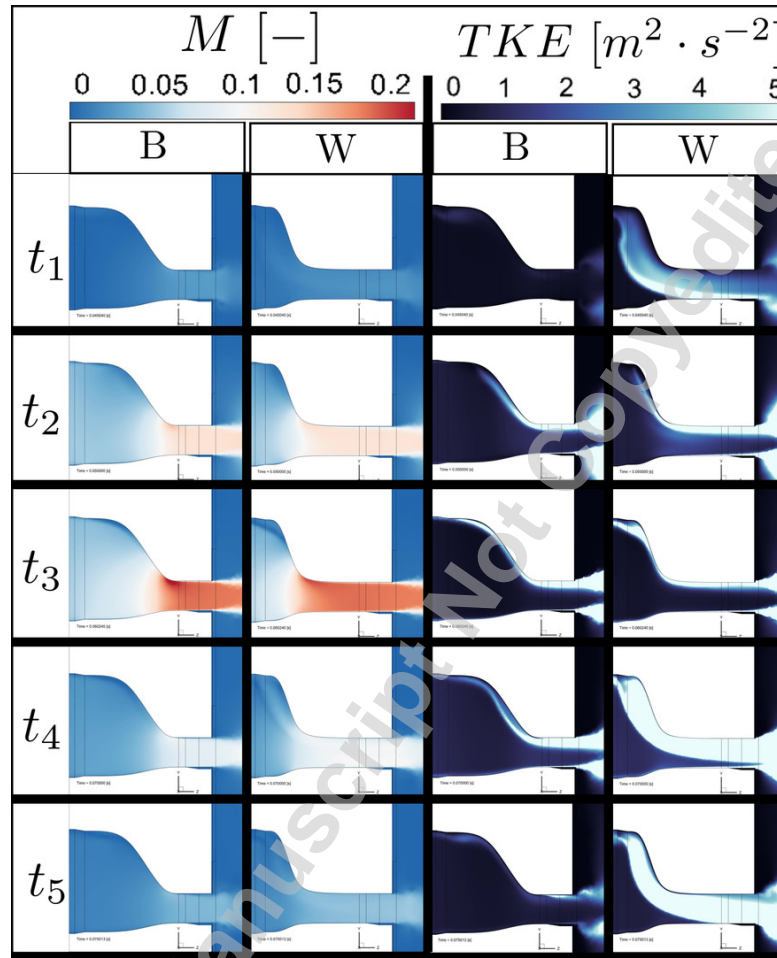samples provide solutions with excitation and not attenuation.

Fig. 9. PERIODIC FLOW FIELD COMPARISON BETWEEN WORST AND BEST CASE AT: $t_1/T_{Period} = 12.5\,\%$, $t_2/T_{Period} = 25\,\%$, $t_3/T_{Period} = 50\,\%$, $t_4/T_{Period} = 75\,\%$, $t_5/T_{Period} = 87.5\,\%$

Moreover, the turbulent kinetic energy allows for detecting the footprint of flow separation. The worst case is unable to face the inlet pulsation and inserts significant region of flow separation to the domain. Thus, its losses are high accompanied with large oscillating outflow by the duct. On the contrary, the best geometry manages to create less notable flow separation preserving the losses at a lower level. The pulsating inflow is guided more efficiently, while the excitation sources are restricted to the ones produced by the shear flow.

In conclusion, the DOE offers a transition duct with successfully restricted pressure losses,

23

while the flow field is excited as less as possible. It must be underlined that the flow field oscillation is enabled by the expansion inside the artificial plenum. This level of unsteadiness would be absent, if a nozzle or a vane was mounted after the transition duct to undertake the expansion process. However, in such wise the samples are tested in conditions even harsher than those which will eventually handle.

4   NUMERICAL ANALYSIS OF NEW EXHAUST SYSTEM

This part of work aims at analysing the new ensemble exhaust system. Starting from the Section 4.1, the flow meshed domain and the numerical configuration of the CFD analysis are presented. Afterwards, Section 4.2 focuses on how a stationary cascade can be evaluated under pulsating inflow. Finally, the transient flow field domain of the vane is investigated in Section 4.3.

4.1   Numerical Set Up

The parametric analysis of the DOE uncovers that the best sample design is the forward loaded with low level of steepness geometry. Thus, this sample is placed as transition duct between the CVC exhaust plenum (*a*) and the HPT vane (*e*) in the configuration of the ensemble exhaust system of Fig. 1. On Fig. 10a and Fig. 10b the new ensemble exhaust system followed by a large artificial plenum is portrayed. In particular, Fig. 10d offers a lateral view of the domain of interest, whereas Fig. 10e provides a top view of the meshed volume upstream of the artificial plenum. Concerning the IGVs, Fig. 10f focuses on the mid–span mesh of the vanes and Fig. 10g gives a detailed view of the leading edge of the stator. The colors of Fig. 10 correspond to the boundary conditions of the Table 6. The spatial periodicity of the flow field allows for analysing only one of the sectors of Fig. 1.

The mesh properties are elected after performing a Grid Dependency Analysis. The results of this analysis are based on the theory by Roache *et al.*[30] and are presented in Table 7. The properties of mass–weighted average Mach number at the outlet of the transition duct and the mass–weighted average stagnation pressure at the outlet of the vane are utilized. In particular, three steady RANS calculations are performed for coarse, medium and fine grid. The original inlet stagnation properties of Fig. 4 which result in the maximum mass flow rate are used for this

purpose. The Grid Convergence Index (GCI) decreases from coarse–medium to medium–fine for the two properties providing values of the asymptotic range of convergence very close to 1. Thus, it can be concluded that the grid size of the medium meshed volume offers grid independent results for the new exhaust system simulation. The total amount of elements of the selected mesh is $\approx 4 \cdot 10^6$.

The URANS equations are solved using a 2nd order accurate density–based implicit solver. Turbulence is calculated with help of k–ω turbulence model proposed by Wilcox [29]. The meshed volume includes an inflation layer close to viscous walls ensuring that y^+ remains below 1. The frequency of the analysis is $25\ Hz$ ($T_{Period} = 0.04\ s$), as it is indicated by the CVC operating period. Nevertheless, the time step of the implicit solver has a sample frequency of $25\ kHz$ to guarantee the proper analysis of the cyclic performance of the new exhaust system. In fact, a second order time advancement scheme is preferred and 20 sub–iterations are needed for every time step to be completed. The boundary conditions which are inserted to the system are the original stagnation properties by the 1D model, as they are depicted on the upper part of Fig. 4.

Boundary Conditions	
Type	Properties
Inlet	Original: $P_t(t)$ & $T_t(t)$
Outlet	$P = 1\ [atm]$
Periodic	-
No–Slip Wall	Adiabatic
Free–Slip Wall	Adiabatic

Table 6.   BOUNDARY CONDITIONS OF NEW EXHAUST SYSTEM

The high pressure level of original boundary conditions combined with the presence of vanes will offer a further acceleration to the flow field comparing the previous case in which only the transition duct samples were tested. Despite of the low reduced frequency of this case as well, the analysis of periodicity criterion via cross correlation is conducted as well. For this purpose, the mass flow, mass–weighted average Mach number and mass–weighted average total temperature
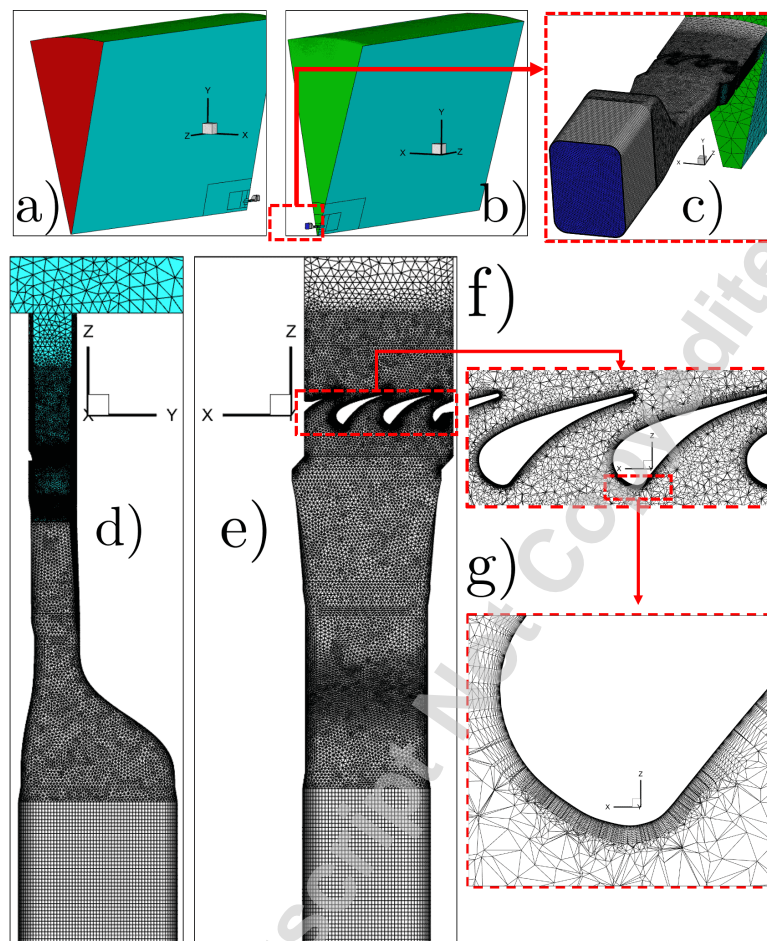
25

Fig. 10. FLOW DOMAIN AND MESHED VOLUME OF NEW EXHAUST SYSTEM

	Grid	Refinement Ratio	GCI	Asymptotic Range of Convergence
$(\mathbf{M})_{\mathbf{Out}}^{\mathbf{Duct}}$	C–M	1.2010	0.257 %	1.004
	M–F	1.2003	0.0366 %	
$(\mathbf{P_t})_{\mathbf{Out}}^{\mathbf{Vane}}$	C–M	1.2010	0.113 %	0.994
	M–F	1.2003	0.0399 %	

Table 7. GRID DEPENDENCY ANALYSIS

of the inlets and outlets of all the enlisted parts of Fig. 1 are monitor through time. The same approach of Section 3.2 is followed. The evolution of minimum, average and maximum values of cross–correlation for zero lag for the three flow variables are portrayed in Fig. 11. It is proved that in the fifth cycle the periodicity is established throughout the whole flow domain of interest.

26
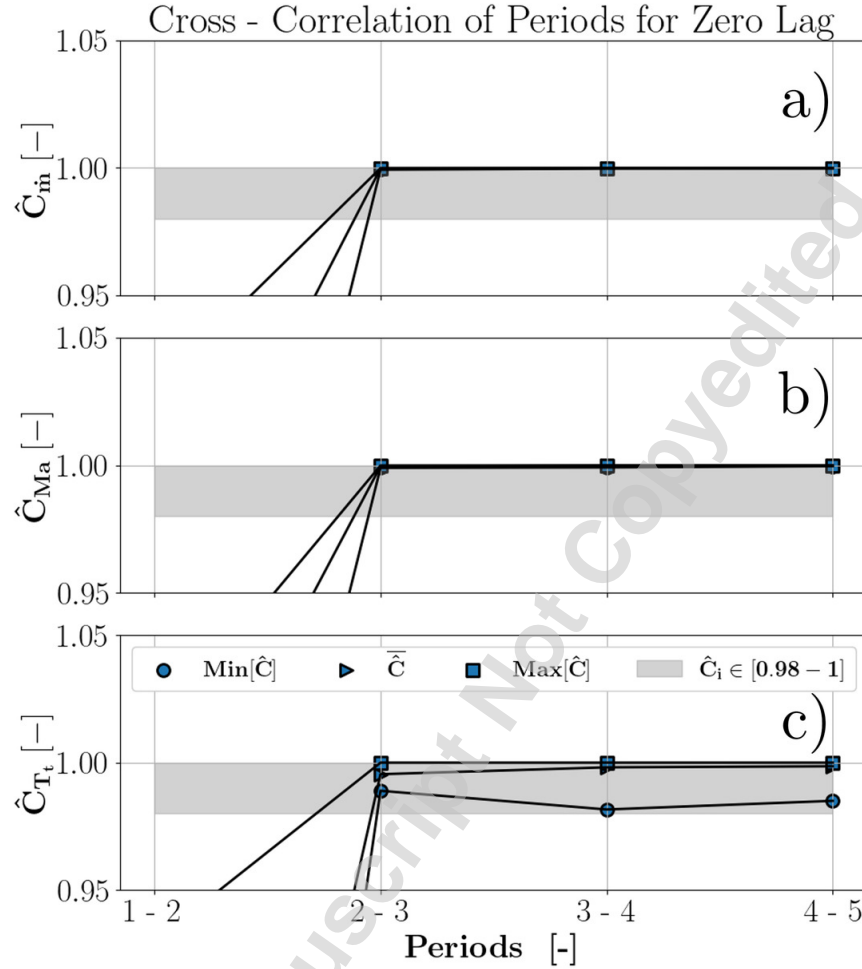
Fig. 11.   ESTABLISHMENT OF PERIODICITY VIA CROSS–CORRELATION CRITERIA FOR ENSEMBLE EXHAUST SYSTEM

4.2   Evaluation of Vanes

Before proceeding on the presentation of the CFD results, it is important to introduce how to evaluate the vane's performance under pulsating inflow. In order to be in accordance with the detailed analysis of the linear cascade of LS–89 VKI [27, 28], the loss coefficient (Eq. 11) and the flow angle deviation coefficient (Eq. 12) should be calculated between the inlet (1) and outlet (2) of the cascade.

27

$$\zeta_v = 1 - \frac{1 - \left(\frac{P_2}{P_{t,\,2}}\right)^{\frac{\gamma-1}{\gamma}}}{1 - \left(\frac{P_2}{P_{t,\,1}}\right)^{\frac{\gamma-1}{\gamma}}} \tag{11}$$

$$\zeta_{\alpha^o} = 1 - \frac{\alpha_2^o}{\alpha_{2,\,metal}^o} \tag{12}$$

The oscillating inflow of the vane imposes difficulties on assessing the aforementioned metrics. The first evaluation can be the mean value of their instantaneous values. This consideration from now on will be mentioned as time average approach. Nonetheless, this would be problematic, as there are specific moments in which the inlet stagnation pressure of the vane is higher than the outlet one. Consequently, the loss coefficient during that moments will be negative. In order to encounter this issue, the flow properties should be averaged before entering into the formulas of Eq. 11 and Eq. 12. As it is suggested by Cumpsty *et al.* [31], extensive properties and total temperature can be mass–weighted averaged, as in Eq. 7. During a period, the cycle average value of a mass–weighted average property is deduced by Eq. 13. Likewise, the cycle mass–weighted average method can be applied on the outlet flow angle of the vane. On the contrary, the stagnation pressure for turbomachinery applications [20, 25, 32] follows the approach of work averaging of Eq. 14.

$$\overline{(\Phi)}^{MA} = \frac{\int_0^\tau (\Phi)^{MA} \cdot \int_A \rho u \, dA \, dt}{\int_0^\tau \int_A \rho u \, dA \, dt} \tag{13}$$

28

$$\overline{(P_t)}^{WA} = \left[\frac{\int_0^\tau \int_A \rho u T_t \, dA \, dt}{\int_0^\tau \int_A \rho u \left[\frac{T_t}{(P_t)^{\frac{\gamma-1}{\gamma}}} \right] dA \, dt} \right]^{\frac{\gamma}{\gamma-1}} \tag{14}$$

Therefore, the cycle average values of stagnation properties at inlet and outlet are now defined. Nevertheless, the static pressure at the outlet of vane oscillates in time as well. One approach can be the time average of area average static pressure of Eq. 15. On this point, all the terms of loss coefficient are defined and the cycle average approach is expressed in Eq. 16 and Eq. 17.

$$\overline{(P)}^{AA} = \frac{1}{\tau \, A} \int_0^\tau \int_A P \, dA \, dt \tag{15}$$

$$(\overline{\zeta})_v^{CA} = 1 - \frac{1 - \left[\frac{(\overline{P_2})^{AA}}{(\overline{P_{t,\,2}})^{WA}} \right]^{\frac{\gamma-1}{\gamma}}}{1 - \left[\frac{(\overline{P_2})^{AA}}{(\overline{P_{t,\,1}})^{WA}} \right]^{\frac{\gamma-1}{\gamma}}} \tag{16}$$

$$(\overline{\zeta})_{\alpha^o}^{CA} = 1 - \frac{(\overline{\alpha_2^o})^{MA}}{\alpha_{2,\,metal}^o} \tag{17}$$

However, for the case of cycle average loss coefficient the cycle average of area averaged static pressure raises doubts. Cumpsty *et al.* [31] underlined that if it is necessary to estimate static properties (*e.g.* total–to–static efficiency) under pulsation, this should be performed in locations that ensure the uniformity of these properties, such as a large plenum tank or open atmosphere. In accordance to this statement, the loss coefficient can be estimated with the help of the outlet

boundary of the artificial plenum (Fig. 10a), where the static pressure is indeed uniform, because the atmospheric pressure is imposed as boundary condition. Hence, an another loss coefficient estimation is found in Eq. 18.

$$(\overline{\zeta})_v^{SA} = \frac{(\zeta_v)^{1 \to out}}{(\zeta_v)^{2 \to out}}$$ (18)

In the last approach the stagnation properties are retrieved by the work averaging, whereas there is no need for averaging the static pressure. This method from now on will be mentioned as split average.

4.3 Results

In Fig. 12, the transient mid–span unwrapped flow field profile of the cascade is portrayed for three different time moments of 20% (t_a), 40% (t_b) and 60% (t_c) of the last cycle. In detail, the three graphs illustrate the Mach number distribution at the exit of the angular duct (part d in Fig. 1) and at the mid–span of the cascade (part e in Fig. 1). The vanes are named P for the case where the profile is split due to periodic boundaries, L for the vane left of the center–line of domain and R for the vane left of the center–line of domain. It is worth to be mentioned that the P vanes are affected by the wake of the upstream junction point (JP) of the different CVC exhaust section segments in every moment. Nonetheless, this effect is successfully restricted only to the wake of the junction and not to a further shear layer generated by increasing the angular dimension through the angular duct (part d in Fig. 1). It is easily observed that the perturbing inflow alternates significantly the operating point of the cascade. The vane's performance shifts from subsonic regime to transonic operation and again back to the subsonic regime. In Fig. 13, the time resolved evolution of the mass–weighted vane outlet Mach number and flow angle are presented. In addition, the pink shaded area illustrates the time window when the vane is choked. In parallel, the numerical results by the 1D model [16, 17] of the existing experimental test rig of the CVC with the exhaust circular nozzle of ISO 9300:2005 provide the time window when the

converging-diverging nozzle is choked (grey shaded area). It is observed that the vane is choked for significantly smaller time of the period than the circular converging–diverging nozzle of the existing test rig. The reason behind this time misalignment emerges from the excessive static pressure drop at the diverging part of the circular nozzle, which is absent in the current case due to the morphology of the LS–89 airfoil.
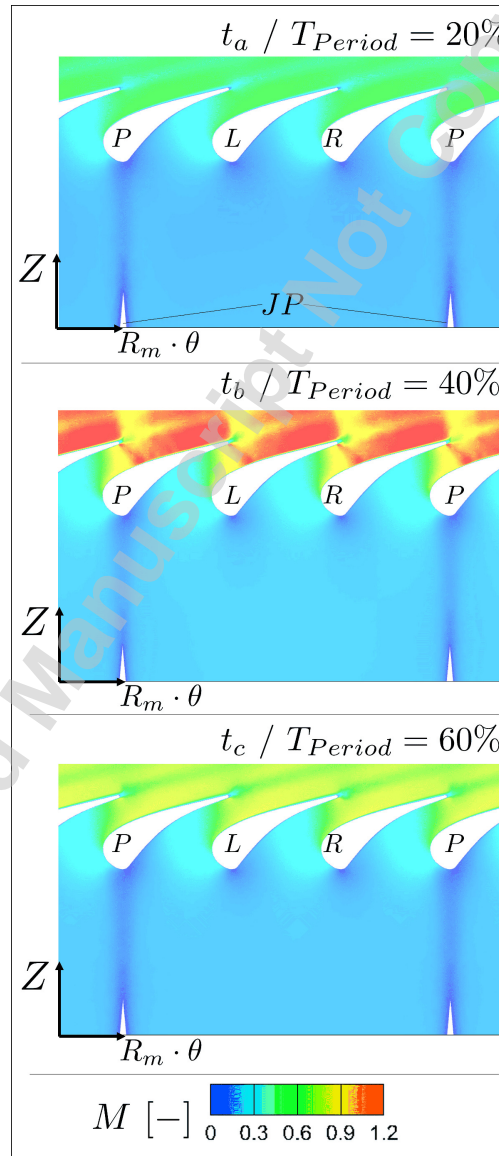

Fig. 12.   PERIODIC FLOW FIELD OF CASCADE: $t_a/T = 20\,\%$, $t_b/T = 40\,\%$ & $t_c/T = 60\,\%$

31

Journal of Engineering for Gas Turbines and Power

It is necessary to determine the outlet isentropic Mach and Reynolds number in order to compare the cycle average vane performance with the steady experimental results [27, 28]. The mass–weighted average (Eq. 13) over a cycle indicates $M_2^{is.} = 0.79$ and $Re_2^{is.} = 0.12 \cdot 10^6$. For the case of the flow angle, the outflow varies its direction with a range of $31 \ deg$. A sudden reduction to the flow angle occurs at $18 \ \%$ of the last cycle, when the inlet stagnation conditions of the vane start to increase. An even harsher reduction takes place at $80 \ \%$ of the last cycle, when the pressure ratio of the vane is significantly reduced. The pulsating conditions affects the outlet flow direction, but the mass–weighted average value of the outlet flow angle for a cycle achieves a high value.
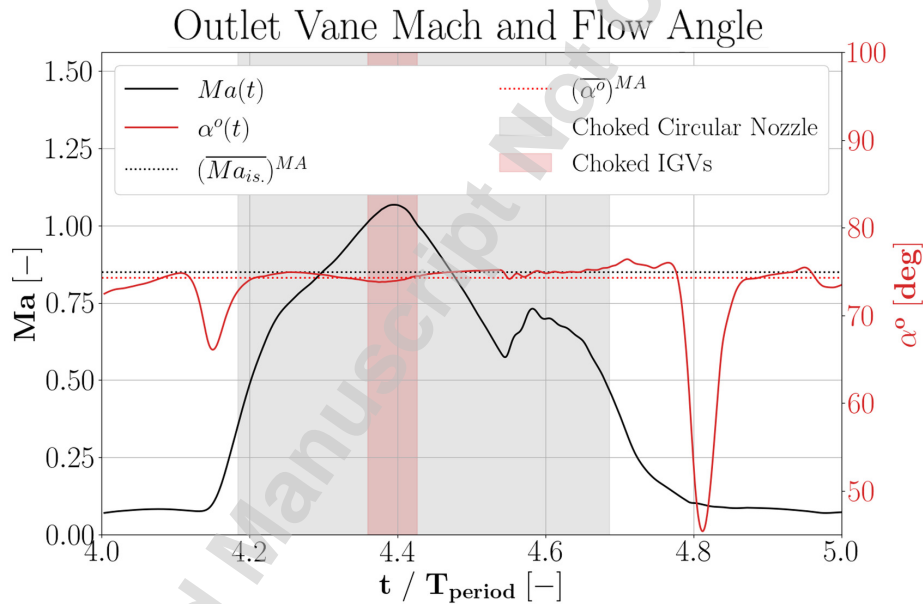
Fig. 13. OPERATIONAL RANGE OF SYSTEM, TRANSIENT MACH NUMBER AND FLOW ANGLE OF VANE OUTLET

The closest set of experimental data to be compared with transient CFD analysis results are those with reported $M_2^{is.} = 0.84$ and $Re_2^{is.} = 10^6$. The mid–span evolution of the pressure along the cascade was experimentally measured [27, 28]. These data are used as a reference for the pulsating analysis of the cascade. It should be underlined that the experimental data have different values of $M_2^{is.}$ and $Re_2^{is.}$ with respect the cycle average properties of the CFD analysis. Moreover, a linear cascade with steady conditions was experimentally investigated, whereas the

32

topic of the current analysis is the simulation of a 3D cascade under the influence of oscillating inflow. Nevertheless, the experimental results can aid to assess the highly unsteady vane's performance. In Fig. 14, the mean evolution of the unsteady load of left (blue), right (green) and periodic (red) vanes are compared with the steady experimental result of the linear cascade at the mid–span. The numerical results correspond to the mid–span of the three vanes which are indicated to Fig. 12. Moreover, the blue shaded area indicates the range of the periodic pressure side (PS) load, while the grey shaded area shows the load variation of the suction side (SS) of the periodic vane. Only the load range of the periodic vane is displayed, as negligible differences are observed comparing the variation of left and right vane. First, the mean load evolution of the right and left vanes agree in the majority of the time. Small differences are noticed with the mean load evolution of the periodic vane. These discrepancies are limited denoting the small influence of the upstream junction point (JP) to the periodic vane performance. Concerning the range, the SS varies approximately twice comparing to PS. The experimental data of PS are inside the margin of the PS operation of the unsteady case. On the other hand, the variation of the SS load seems to differ from the experiments in the fore part of the vane. In fact, the SS of the linear experimental cascade is unaffected by the development of the secondary flows (*e.g.* passage vortex), as the linear vane passage is not characterized by curved hub and tip endwalls. As a result, centrifugal forces in the radial direction of the cascade are missing preventing the development of secondary flows. However, the endwalls of the cascade of the new exhaust system are not linear, but curved. Considering the perturbing inflow, it can be safely presumed that the predominant and periodic presence of the secondary flows deteriorates the acceleration of the vane. Therefore, a straight comparison between the linear cascade with steady inflow and the 3D vane under pulsating inlet conditions should take into consideration the strong presence of the secondary flows for the latter case.

Afterwards, the performance of the vane is assessed in terms of loss coefficient (Eq. 11) and flow angle deviation coefficient (Eq. 12) for a cycle. These two metrics are expressed as time average of their instantaneous values and as cycle average values following Eq. 16 and Eq. 17 respectively. In particular for the case of loss coefficient, the third expression of split average in
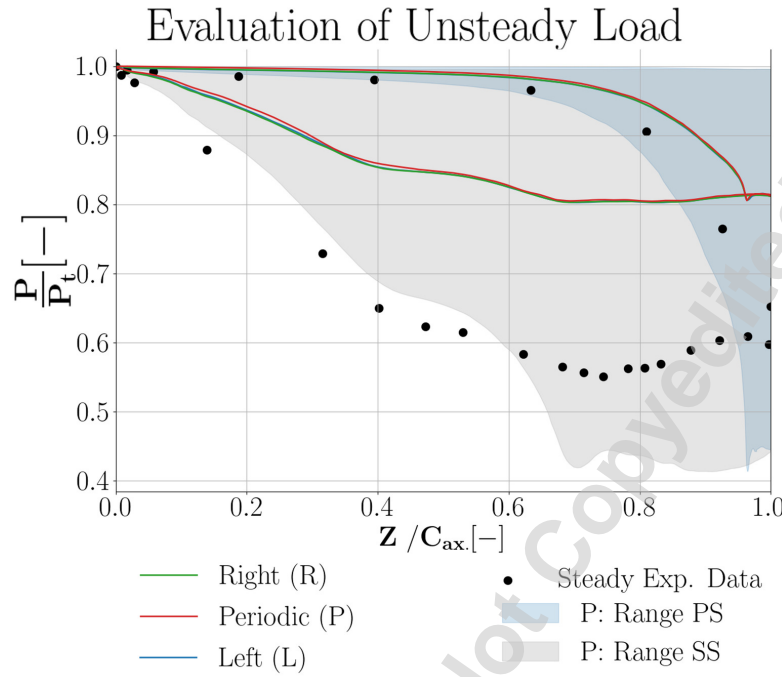
33

Fig. 14. COMPARISON OF UNSTEADY VANES LOAD ($M_2^{is.} = 0.79$, $Re_2^{is.} = 0.12 \cdot 10^6$) WITH STEADY EXPERIMENTAL RESULTS ($M_2^{is.} = 0.84$, $Re_2^{is.} = 10^6$)

Eq. 18 is added. In Table 8, the aforementioned aerodynamic performance evaluation of LS–89 during the last analysed period is placed. Concerning the loss coefficient, the time average value underestimates the produced losses, while the cycle average and split average seems to agree. On the other hand, the time average of flow angle deviation coefficient is significantly higher comparing the one by the cycle average approach. In Fig. 15, the loss coefficient and flow angle deviation coefficient are compared with the available experimental data. The unsteady case rises the level of losses and the loss coefficient exceeds the experimental tested range. This excitation can be attributed to the pulsating flow field highly affected by centrifugal forces which are absent for the experimental results of steady inflow. For the case of the flow angle, the values approach the observed experimental range. As a matter of fact, the pulsating inflow and the development of the secondary flows do not incommode the vane to provide the prescribed metal angle to the flow field. In conclusion, the vane exhibits almost 10.5% of loss coefficient while the outlet flow angle deviates only 0.9% from the prescribed outlet metal angle. The results are very optimistic if ones considers the placement of a rotor blade after the vane. During a cycle, the transition duct and the

34

vane are able to provide a flow field that in average is characterized by small amount of losses, while the flow direction is kept close to the defined metal angle value.

Property	Time Average	Cycle Average	Split Average
$\zeta_{\mathbf{v}}$	0.09	0.105	0.1
ζ_{α^o}	0.025	0.009	-

Table 8.   AERODYNAMIC PERFORMANCE OF CASCADE
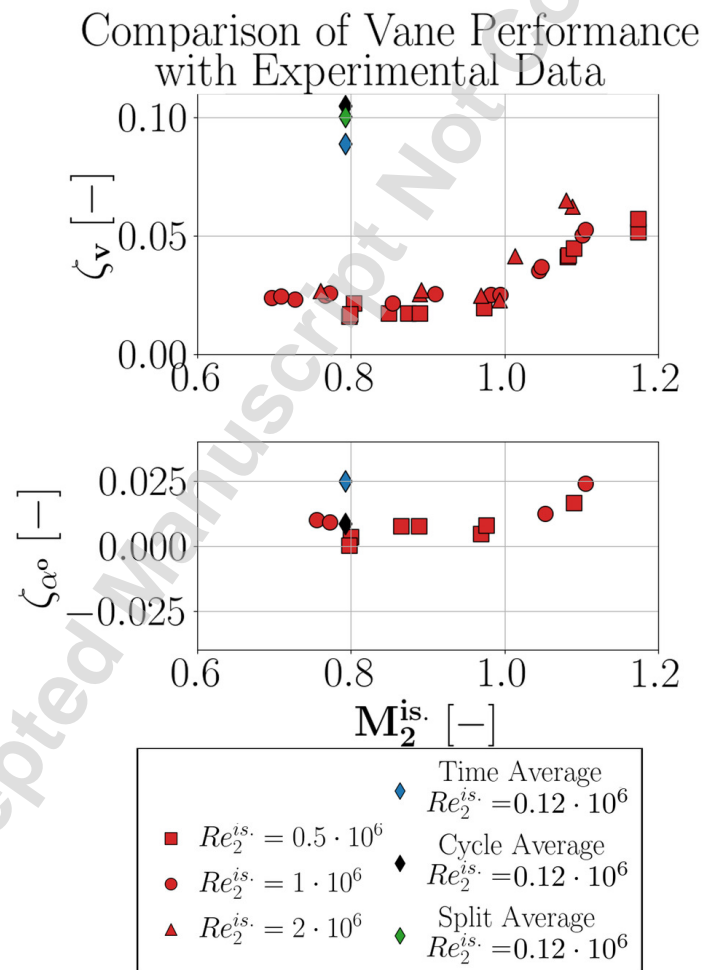
Fig. 15.   COMPARISON OF VANE PERFORMANCE UNDER PULSATION WITH EXPERIMENTAL RESULTS

35

In the end, the pressure losses and attenuation evaluation is performed over a cycle. The same approach of Section 3.4 is followed for the purposes of the last part of the analysis as well. The results of this study are depicted in the Fig. 16. For each part of the exhaust domain, the stagnation pressure losses of Eq. 8 and the damping factor of Eq. 9 are calculated. In particular, two considerations are made. First, the component evaluation (CO) is performed in which the inlet of each component is compared to its outlet. In addition, the cumulative evaluation (CU) is conducted in which every outlet of the components is compared with the inlet of the domain. In terms of total pressure losses, 2.96 % of stagnation pressure is lost through the system, while the cascade is responsible for the vast majority of this value. On the contrary, the stagnation pressure signal is attenuated at the level of 10.6 %. Again, the vane plays a predominant role on the attenuation of the field. In parallel, the plenum excites the flow field, while the transition duct and the angular duct achieve attenuation of low level. This conclusion corroborates the statement that
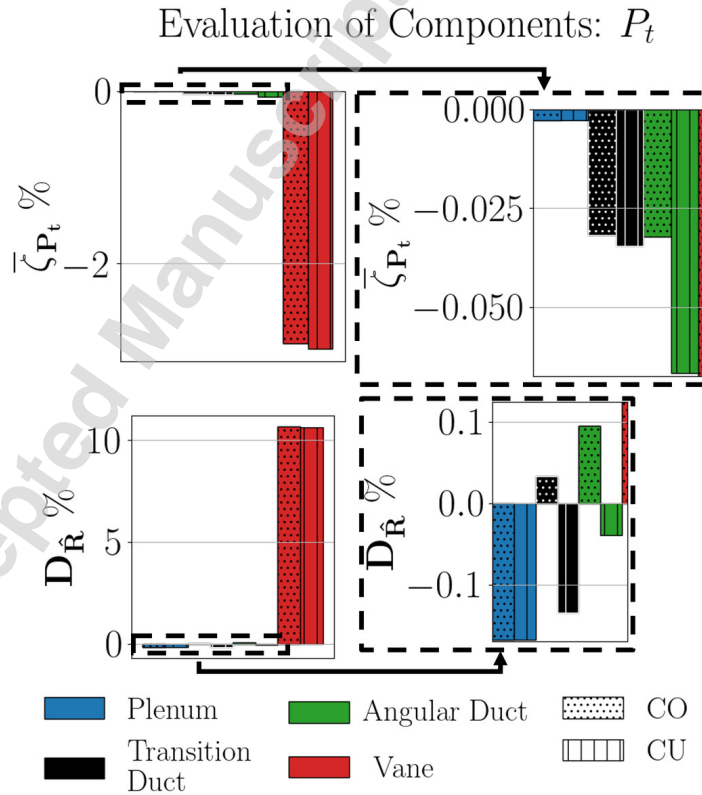
Fig. 16.   EVALUATION OF LOSSES AND OSCILLATIONS OF COMPONENTS

36

the flow field excitation by the samples during the DOE analysis will be absent in the case of the ensemble exhaust system analysis. In fact, excitation in DOE occurs due to the subsequent shear flow of direct expansion to the artificial plenum and not due to the shape of the transition duct's endwalls. In summary, the new design of exhaust system accomplishes high level of excitation with limited induced losses.

5 CONCLUSIONS

The present activity focuses on the design and the analysis of a new exhaust system after CVC by numerical means. The new outlet section connects the CVC with the LS–89 VKI cascade through a transition duct. The first part of the activity is devoted to the numerical parametric analysis of the transition duct designs. It is introduced the geometrical parametrization of the transition duct and with the help of the full factorial design method of 3 levels a DOE of 81 geometries is offered. For every case URANS simulations are performed. The shear flow of the expansion inside the artificial plenum and not the samples' endwalls is the responsible for the excitation of the flow field for every tested geometry. Backward loaded samples exhibit higher losses, while the best geometry is a forward loaded sample of low level of steepness. In the end, a straight comparison of the flow field between the best and the worst sample is conducted uncovering the difficulties of the steep backward loaded geometries to handle the induced boundary layer separation by the modified endwalls.

The second part of this manuscript concerns the numerical analysis of the ensemble exhaust system. The best sample derived by the parametric analysis is utilized as transition duct of the new exhaust system. The oscillating inflow alters the operating point of the cascade from the subsonic range to the transonic regime and then back to the subsonic operation. The performance of the cascade is evaluated in terms of loss coefficient and flow angle deviation coefficient. The vane exhibits 10.5 % of loss coefficient while keeps the flow angle deviation only to 0.9 %. Afterwards, the new exhaust system is evaluated in terms of produced losses and its ability to attenuate the flow field. The system achieves 10.6 % of attenuation while inserts only 2.96 % of losses. In particular, the transition duct manages to induce negligible losses with a small contribution on flow

37

field attenuation.

In the end, a comparison of the pulsating 3D cascade performance with the experimental data of the linear cascade under steady inflow is performed. The loss coefficient of the simulation is increased with respect the experimental results of the linear cascade. Nevertheless, a direct comparison of the performance between the numerical unsteady analysis and the steady experimental campaign should take into consideration the absence of the secondary flows in the latter case. In spite of the oscillating inflow and the strong presence of centrifugal forces, the cycle average coefficient of flow deviation remains inside the range of the experiments. The limited amount of losses accompanied by the large level of attenuation and the ability of the vane to provide an outflow with a direction very close to the prescribed metal angle uncover particularly encouraging prospects for the placement of a rotor in the aft part of the new exhaust system. Therefore, future efforts will focus on the integration of a rotor after the LS–89 vane in order to numerically investigate the amount of the produced work that this unconventional combustor can provide. In addition, the best sample of the transition duct will be manufactured and tested in order to evaluate for the first time experimentally the peculiar outflow of the CVC.

ACKNOWLEDGMENTS

REFERENCES

[1] Heiser, W. H., and Pratt, D. T., 2002, "Thermodynamic cycle analysis of pulse detonation engines," *Journal of Propulsion and Power,* **18**(1), Jan., p. 68–76.

[2] Nordeen, C. A., 2013, "Concepts and definitions: Efficiency of detonation," In *Thermodynamics of a rotating detonation engine*. University of Connecticut, December, ch. 1, pp. 10–15 PhD thesis.

38

[3] Stathopoulos, P., Vinkeloe, J., and Paschereit, C. O., 2015, "Thermodynamic evaluation of constant volume combustion for gas turbine power cycles," In Numerical Set Updings of the 11th International Gas Turbine Congress, pp. 15–20.

[4] Sousa, J., Paniagua, G., and Collado Morata, E., June 2017, "Thermodynamic analysis of a gas turbine engine with a rotating detonation combustor," *Applied Energy,* **195**, June, p. 247–256.

[5] Ciccarelli, G., and Dorofeev, S., 2008, "Flame acceleration and transition to detonation in ducts," *Progress in Energy and Combustion Science,* **34**(4), Aug., p. 499–550.

[6] Wolański, P., 2013, "Detonative propulsion," *Proceedings of the Combustion Institute,* **34**(1), p. 125–158.

[7] Roy, G., Frolov, S., Borisov, A., and Netzer, D., 2004, "Pulse detonation propulsion: challenges, current status, and future perspective," *Progress in Energy and Combustion Science,* **30**(6), Jan., p. 545–672.

[8] Ma, J. Z., Luan, M.-Y., Xia, Z.-J., Wang, J.-P., Zhang, S.-j., Yao, S.-b., and Wang, B., 2020, "Recent progress, development trends, and consideration of continuous detonation engines," *AIAA Journal,* **58**(12), Dec., p. 4976–5035.

[9] Hishida, M., Fujiwara, T., and Wolanski, P., 2009, "Fundamentals of rotating detonations," *Shock Waves,* **19**(1), Apr., p. 1–10.

[10] Lu, F. K., and Braun, E. M., 2014, "Rotating detonation wave propulsion: Experimental challenges, modeling, and engine concepts," *Journal of Propulsion and Power,* **30**(5), Sept., p. 1125–1142.

[11] Akbari, P., Nalim, R., and Mueller, N., 2006, "A review of wave rotor technology and its applications," *Journal of Engineering for Gas Turbines and Power,* **128**(4), Oct., p. 717–735.

[12] Bobusch, B. C., Berndt, P., Paschereit, C. O., and Klein, R., 2014, "Shockless explosion combustion: An innovative way of efficient constant volume combustion in gas turbines," *Combustion Science and Technology,* **186**(10–11), Nov., p. 1680–1689.

[13] Boust, B., Michalski, Q., and Bellenoue, M., 2016, "Experimental investigation of ignition and combustion processes in a constant-volume combustion chamber for air-breathing propul-

39

sion," In 52nd AIAA/SAE/ASEE Joint Propulsion Conference, AIAA, p. 4699.

[14] Labarrere, L., Poinsot, T., Dauptain, A., Duchaine, F., Bellenoue, M., and Boust, B., Oct. 2016, "Experimental and numerical study of cyclic variations in a constant volume combustion chamber," *Combustion and Flame,* **172**, Oct., p. 49–61.

[15] Boust, B., Bellenoue, M., and Michalski, Q., 2022, "Pressure gain and specific impulse measurements in a constant-volume combustor coupled to an exhaust plenum," In Active Flow and Combustion Control 2021, Springer, pp. 3–15.

[16] Gallis, P., Misul, D. A., Salvadori, S., Bellenoue, M., and Boust, B., 15-19 August, 2022, "Development and validation of a 0-d/1-d model to evaluate pulsating conditions from a constant volume combustor," In Joint Meeting of International Workshop on Detonation for Propulsion (IWDP) and International Constant Volume and Detonation Combustion Workshop (ICVDCW).

[17] Gallis, P., Misul, D. A., Bellenoue, M., Boust, B., and Salvadori, S., 2024, "Development of 1d model of constant-volume combustor and numerical analysis of the exhaust nozzle," *Energies,* **17**(5), p. 1191.

[18] Liu, Z., Braun, J., and Paniagua, G., 2017, "Performance of axial turbines exposed to large fluctuations," In 53rd AIAA/SAE/ASEE Joint Propulsion Conference, American Institute of Aeronautics and Astronautics.

[19] Glaser, A., Caldwell, N., and Gutmark, E., 2006, "Performance measurements of a pulse detonation combustor array integrated with an axial flow turbine," In 44th AIAA Aerospace Sciences Meeting and Exhibit, American Institute of Aeronautics and Astronautics.

[20] George, A. S., Driscoll, R., Gutmark, E., and Munday, D., 2014, "Experimental comparison of axial turbine performance under steady and pulsating flows," *Journal of Turbomachinery,* **136**(11), Nov., p. 111005.

[21] Anand, V., St. George, A., Knight, E., and Gutmark, E., 2019, "Investigation of pulse detonation combustors — axial turbine system," *Aerospace Science and Technology,* **93**, Oct., p. 105350.

[22] Fernelius, M., Gorrell, S. E., Hoke, J., and Schauer, F., 2013, "Effect of periodic pressure

pulses on axial turbine performance," In 49th AIAA/ASME/SAE/ASEE Joint Propulsion Con-
ference, AIAA, p. 3687.

[23] Fernelius, M. H., and Gorrell, S. E., 2020, "Mapping efficiency of a pulsing flow-driven turbine,"
Journal of Fluids Engineering, **142**(6), Mar.

[24] Ni, R. H., Humber, W., Ni, M., Sondergaard, R., and Ooten, M., 2013, "Performance estima-
tion of a turbine under partial-admission and flow pulsation conditions at inlet," In Volume 6C:
Turbomachinery, GT2013, American Society of Mechanical Engineers.

[25] Xisto, C., Petit, O., Grönstedt, T., Rolt, A., Lundbladh, A., and Paniagua, G., 2018, "The
efficiency of a pulsed detonation combustor–axial turbine integration," *Aerospace Science
and Technology,* **82–83**, Nov., p. 80–91.

[26] Liu, Z., Braun, J., and Paniagua, G., 2020, "Integration of a transonic high-pressure turbine
with a rotating detonation combustor and a diffuser," *International Journal of Turbo amp;
Jet-Engines,* **0**(0), July.

[27] Arts, T., De Rouvroit, M. L., and Rutherford, A., 1990, *Aero-thermal investigation of a highly
loaded transonic linear turbine guide vane cascade* von Karman Institute for Fluid Dynamics.

[28] Arts, T., and De Rouvroit, M. L., 1990, "Aero-thermal performance of a two dimensional
highly loaded transonic turbine nozzle guide vane: A test case for inviscid and viscous flow
computations," In Volume 1: Turbomachinery, GT1990, American Society of Mechanical
Engineers.

[29] Wilcox, D. C., 2008, "Formulation of the k-w turbulence model revisited," *AIAA Journal,*
46(11), Nov., p. 2823–2838.

[30] Roache, P. J., 1998, "Verification of codes and calculations," *AIAA Journal,* **36**(5), May,
p. 696–702.

[31] Cumpsty, N. A., and Horlock, J. H., 2005, "Averaging nonuniform flow for a purpose," *Journal
of Turbomachinery,* **128**(1), Feb., p. 120–129.

[32] Suresh, A., Hofer, D. C., and Tangirala, V. E., 2011, "Turbine efficiency for unsteady, periodic
flows," *Journal of Turbomachinery,* **134**(3), July.

Journal of Engineering for Gas Turbines and Power

LIST OF FIGURES

LIST OF TABLES